

Ultrafast Pulsed Laser Induced Nanocrystal Transformation in Colloidal Plasmonic Vesicles

Mohammad Rezaul Karim, Xiuying Li, Peiyuan Kang, Jaona Randrianalisoa, Dineli Ranathunga, Steven Nielsen, Zhenpeng Qin,* and Dong Qian*

Plasmonic vesicle consists of multiple gold nanocrystals within a polymer coating or around a phospholipid core. As a multifunctional nanostructure, it has unique advantages of assembling small nanoparticles (<5 nm) for rapid renal clearance, strong plasmonic coupling for ultrasensitive biosensing and imaging, and near-infrared light absorption for drug release. Thus, understanding the interaction of plasmonic vesicles with light is critically important for a wide range of applications. In this paper, a combined experimental and computational study is presented on the nanocrystal transformation in colloidal plasmonic vesicles induced by the ultrafast picosecond pulsed laser. Experimentally observed merging and transformation of small nanocrystals into larger nanoparticles when treated by laser pulses is first reported. The underlying mechanisms responsible for the experimental observations are investigated with a multiphysics computational approach featuring coupled electromagnetic/molecular dynamics simulation. This study reveals for the first time that combined nanoparticle heating and laser-enhanced Brownian motion is responsible for the observed nanocrystal merging. Correspondingly, laser fluence, interparticle distance, and presence of water are identified as the most important factors governing the nanocrystal transformation. The guidelines established from this study can be employed to design a host of biomedical and nanomanufacturing applications involving laser interaction with plasmonic nanoparticles.

navigating complex biological systems requires nanostructure designs with enhanced functionality and responsiveness, for instance, by incorporating multiple features into a single nanosystem.^[3] Plasmonic vesicle is an example of the multifunctional nanostructures, usually made of small plasmonic gold nanoparticles and a lipid or polymer core vesicle.^[3–5] Plasmonic vesicles provide several functionalities and advantages compared with either plasmonic nanoparticle or organic vesicle alone. For instance, they can be used as an imaging contrast due to the plasmonic absorption of gold,^[6] optically addressable delivery systems,^[7] efficient agents for photothermal therapy of cancer,^[8] and importantly renal clearance of small gold nanoparticles (<5 nm).^[9] Researchers have demonstrated that plasmonic vesicles can enable ultraviolet (UV) or near-infrared (NIR) light-induced cargo release.^[10] Our recent studies demonstrated the feasibility of nonthermal, ultrafast, and highly controllable uncaging of biomolecules from plasmonic gold-coated liposomes by NIR laser pulses.^[11] Thus, understanding the

interaction of plasmonic vesicles with lasers, especially with ultrafast pulsed laser when gold nanoparticles can reach very high localized temperatures, is critically important for a wide range of applications.


Nanoparticles go through conformational changes when activated by ultrafast pulsed laser.^[12,13] Notably, it is

1. Introduction

The last decade has witnessed extensive investigations on the effects of the nanoparticle size, shape, and surface chemistry on the complex interactions between nanomaterials and the biological system.^[1,2] These studies have revealed that

M. R. Karim, Dr. X. Li, P. Kang, Prof. Z. Qin, Prof. D. Qian
Department of Mechanical Engineering
University of Texas at Dallas
800 West Campbell Rd., Richardson, TX 75080, USA
E-mail: Zhenpeng.Qin@utdallas.edu; dong.qian@utdallas.edu

Prof. J. Randrianalisoa
Groupe de Recherche en Sciences pour L'Ingénieur (GRESPI EA 4694)
University of Reims Champagne-Ardenne
Reims Cedex 2, 51687, France

 The ORCID identification number(s) for the author(s) of this article can be found under <https://doi.org/10.1002/adom.201800726>.

D. Ranathunga, Prof. S. Nielsen
Department of Chemistry and Biochemistry
University of Texas at Dallas
800 West Campbell Rd., Richardson, TX 75080, USA

Prof. Z. Qin
Department of Bioengineering
University of Texas at Dallas
800 West Campbell Rd., Richardson, TX 75080, USA

Prof. Z. Qin
Department of Surgery
University of Texas at Southwestern Medical Center
5323 Harry Hines Blvb., Dallas, TX 75390, USA

DOI: 10.1002/adom.201800726

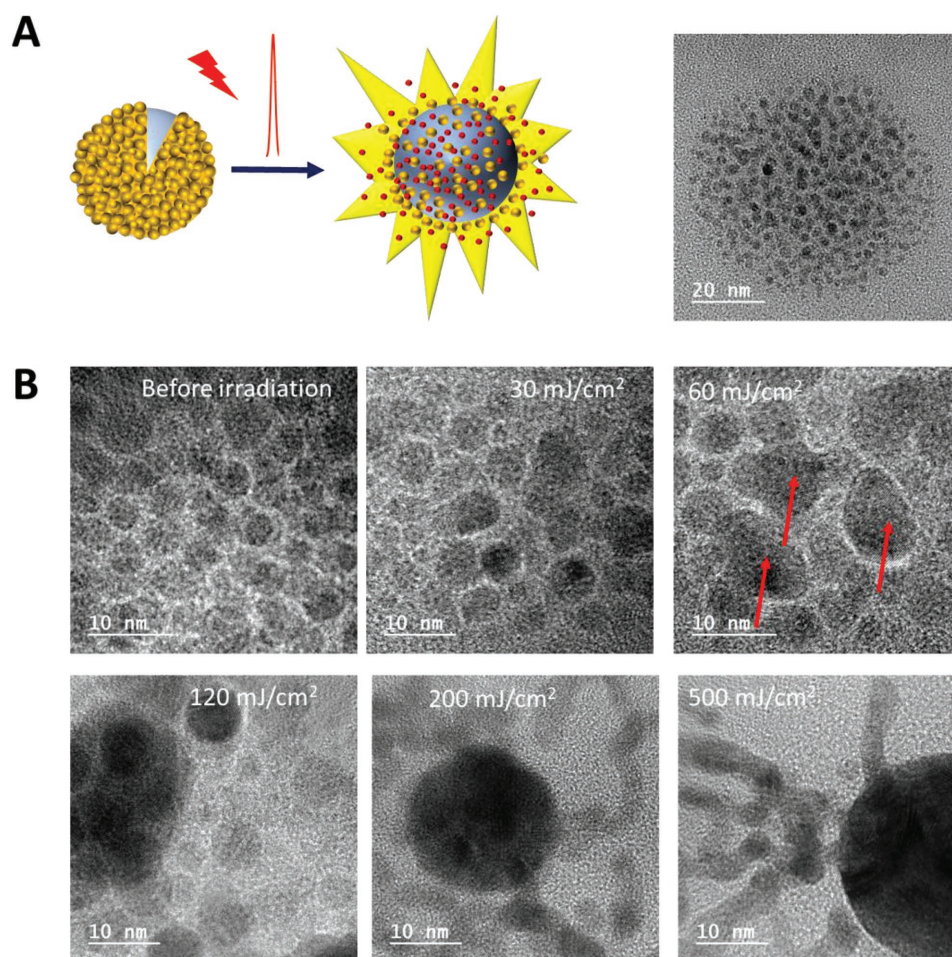


Figure 1. Experimental observation of ultrafast pulsed laser induced nanocrystal transformation. A) Schematic of the laser pulse induced burst release of drug (red dots) using plasmonic gold-coated liposome vesicle. Gold nanoparticles are highlighted by yellow particles. Right: transmission electron microscopy (TEM) image of gold nanoparticle coated liposome; B) transmission electron microscopy observation of nanocrystal transformation upon laser pulse treatments of different laser fluences. The arrows indicate merged nanoparticles.

well-known that ultrafast pulsed laser changes gold nanorods into spheres even at very low laser intensities.^[14] Furthermore, ultrafast pulsed laser can lead to head-to-head assembly of nanorods,^[15] reshaping of nanorods to obtain ultranarrow surface plasmon resonances,^[16] and merging of nanoparticle aggregates.^[17] However, the mechanism of nanocrystal transformation and merging is largely unclear for plasmonic vesicles subjected to ultrafast pulsed laser. The goal of this study is to investigate the conditions and mechanisms of nanocrystal transformation, in particular for plasmonic vesicles that assemble plasmonic gold nanoparticles in close proximity. Our study reveals that laser-induced nanocrystal transformation is strongly dependent on both the inter-nanoparticle distance and laser fluence. More importantly, the nanocrystal merging requires the presence of water. Beyond biomedical applications, the fundamental understanding of laser-induced nanocrystal transformation is important as it can lead to new nanomanufacturing approaches to produce nanostructures in large scales since laser processing can be streamlined.^[16]

2. Result and Discussion

We first experimentally observed the nanocrystal transformation in plasmonic gold-coated liposomes due to ultrafast pulsed laser treatment. Gold-coated liposomes were synthesized following a liposome metallization procedure reported previously.^[11,18] Briefly, very small gold nanoparticles with diameters in the range of 3–5 nm were densely deposited onto the liposome surface (Figure 1A). We have used this plasmonic vesicle and picosecond laser pulses to construct a ultrafast compound release system for signaling molecules including neurotransmitters due to the fast release speed.^[11] After single laser pulse treatment at 30 mJ cm⁻², no obvious change was observed for gold nanoparticles on the plasmonic vesicles (Figure 1B). However, at laser fluence above 30 mJ cm⁻², different degrees of nanocrystal transformation appeared. Specifically, several gold nanoparticles (2–4) appeared to merge at 60 mJ cm⁻², and very large gold nanocrystals (size > 10 nm) appeared at 200 and 500 mJ cm⁻². This laser fluence dependent nanocrystal transformation is surprising since the picosecond laser treatment

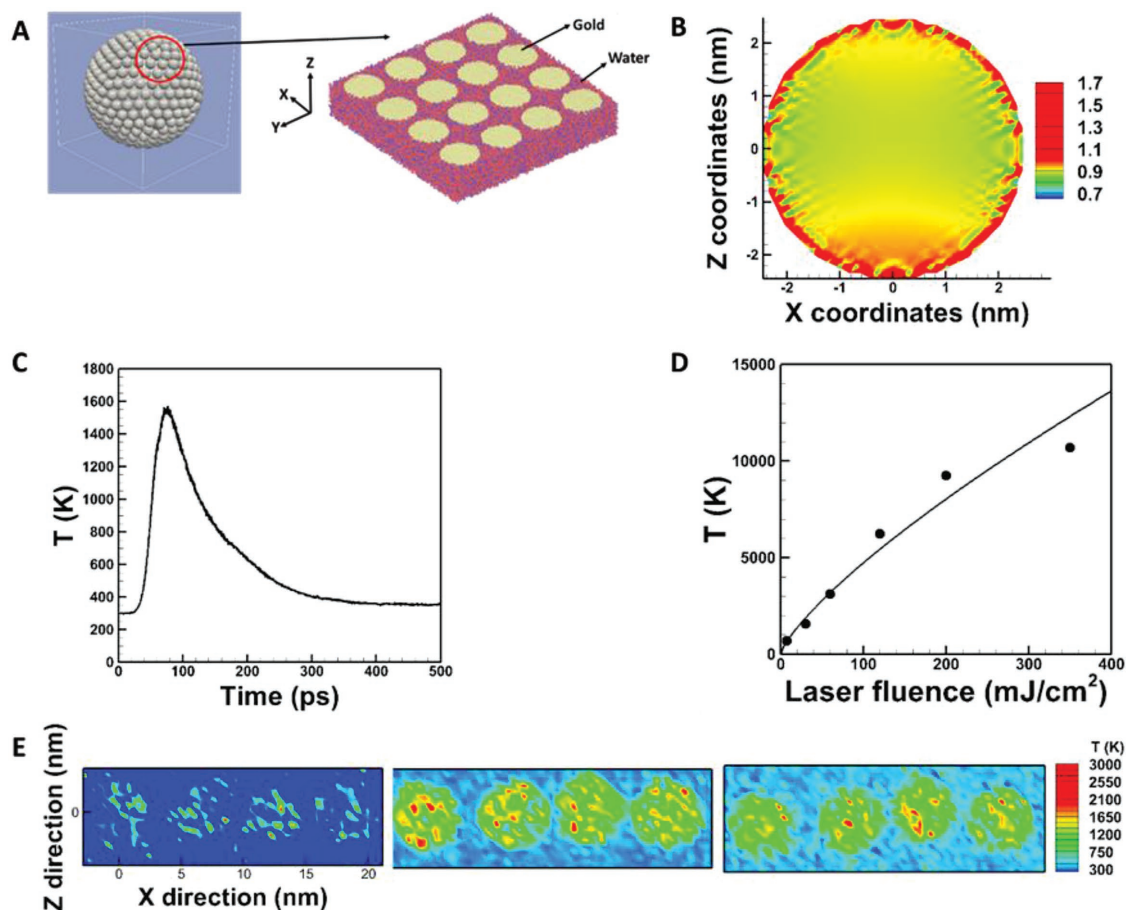


Figure 2. Ultrafast pulsed laser heating of plasmonic nanoparticles leads to rapid temperature increase and uniform temperature distribution. A) Schematic of gold nanoparticle-coated vesicle and molecular dynamic model setup that consists of gold nanoparticle array and water molecules. Cross section along Z direction is shown for better visualization. B) Normalized power density distribution along $Y=0$ plane. C) Average gold nanoparticle temperature as a function of time at 30 mJ cm^{-2} . D) Dependence of peak temperature in gold nanoparticle as a function of laser fluence (mJ cm^{-2}). E) Instantaneous temperature distributions along center of Y plane at 37 ps (left), 75 ps (middle), and 100 ps (right) at laser fluence of 30 mJ cm^{-2} .

leads to intense nanoparticle heating and subsequent nanoscale cavitation, known as plasmonic nanobubbles, to break apart the plasmonic vesicles. The presence of nanobubbles was confirmed by optically measuring the intense scattering due to the vapor/water contrast in the refractive index.^[11] Instead of separating the gold nanoparticles by nanoscale cavitation, the unexpected observation of nanocrystal merging is intriguing and thus led us to further investigate the underlying mechanism.

Next, we performed molecular dynamic simulations to investigate the mechanism of nanocrystal transformation under conditions similar to plasmonic vesicles. The plasmonic vesicle can be approximated as an array of gold nanoparticles around a spherical vesicle core.

To control the simulation domain and at the same time capture key features of a plasmonic vesicle, we selected a small area on the plasmonic vesicle and built a simulation domain with a 4×4 planar array of 5 nm gold nanoparticles separated by a gap that ranges from 1 to 3 nm (Figure 2A). We first calculated the electromagnetic field distribution within nanoparticles by using the discrete dipole approximation (DDA) method. This information was then used to obtain the detailed heat generation distribution within the gold nanoparticles. The heat

generation on the nanoparticle surface was found to be much higher than the interior of the nanoparticle (70% difference in power density, Figure 2B). We then examined the temperature distribution within gold nanoparticles. The average gold nanoparticle temperature increased quickly with the picosecond laser pulse (Figure 2C) and reached higher temperatures at higher laser fluence (Figure 2D and Figure S1, Supporting Information). Although strong localized electromagnetic field and thus power density is higher at polar sides of the nanoparticle (Figure 2B) given that the laser pulse was applied toward the positive z-direction, the simultaneous heat transfer within the nanoparticles quickly redistributes the heat as time evolves (Figure 2E, temperature distributions at 37, 75, and 100 ps).

We further investigated the conditions for nanocrystal transformation with the above computational framework. Gold nanoparticle merging and transformation showed a strong dependence on the picosecond laser fluence. Specifically, no merging was observed at low laser fluence (7.5 mJ cm^{-2}). From 30 to 120 mJ cm^{-2} , different degrees of nanoparticle merging and transformation were observed (Figure 3A). During merging, gold nanoparticles came closer to each other and a neck was formed between them (Figure 3B). The merged

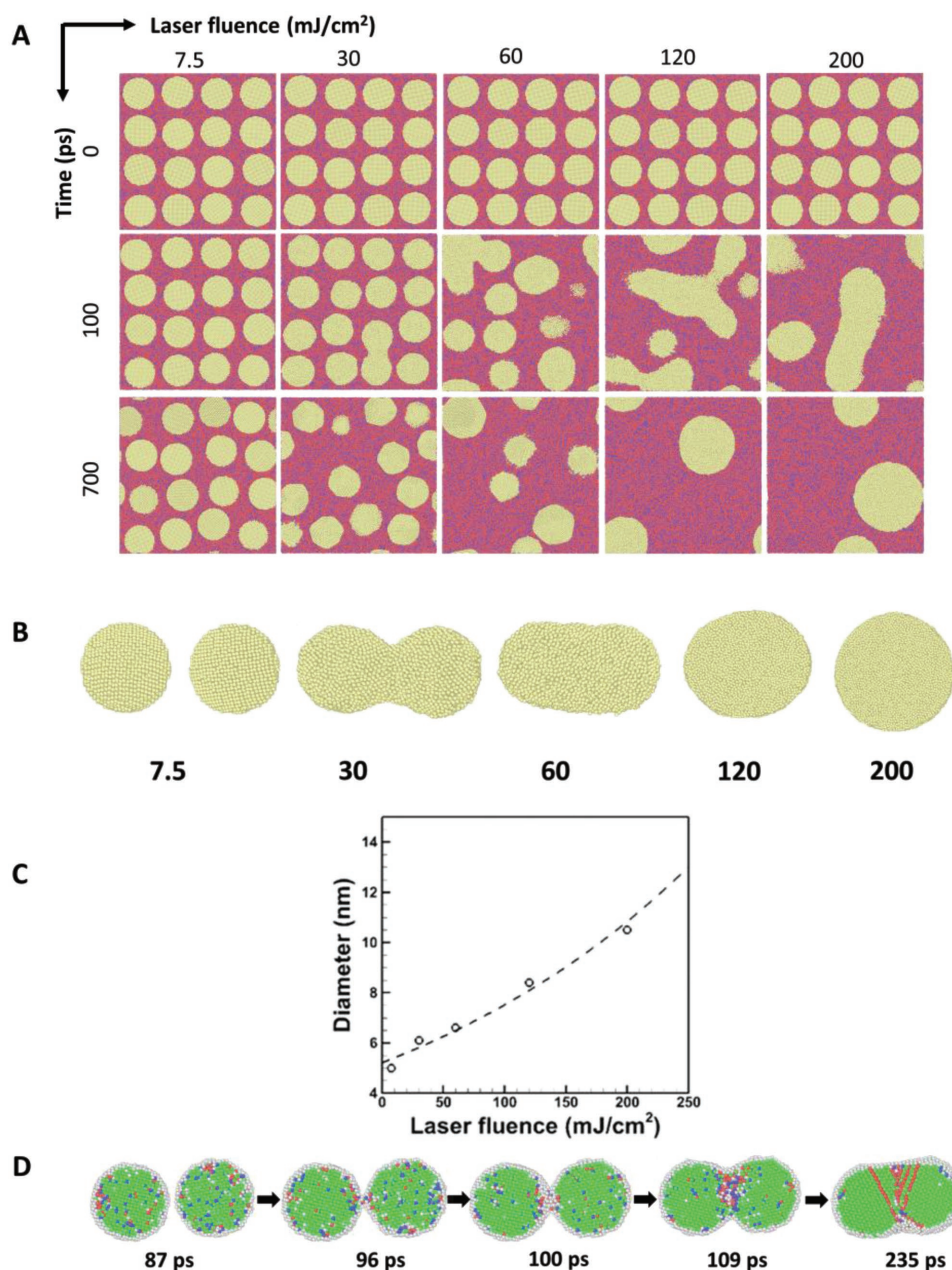


Figure 3. Coupled electromagnetic/molecular dynamic simulation of laser fluence-dependent nanocrystal transformation and merging. A) Snapshots at different laser fluences and time points. Each column represents snapshots at one laser fluence. From left to right: 7.5, 30, 60, 120, and 200 mJ cm⁻² at 0, 100, and 700 ps (top, middle, and bottom rows). B) Morphologies of merged gold nanoparticles at different laser pulse fluences (mJ cm⁻²). C) Size of the largest growing nanoparticles increases with laser pulse fluences (mJ cm⁻²). D) Nanostructure evolutions of gold nanoparticles merging (green, gray/violet, and red colors stand for fcc, disordered, and stacking faults atoms, respectively).

gold nanoparticles changed from ellipsoidal to spherical shape depending on the laser fluence. As the laser fluence increases, the size of the largest growing nanoparticle also increases (Figure 3C). At very high laser fluence (200 mJ cm⁻²), significant nanoparticle melting, fragmentation, and presence of large nanoparticle aggregates were observed (Figure 3A and Figure S2, Supporting Information). Melting points of simulated gold nanoparticles were reported to range from 615 to 1115 K depending on nanoparticle size,^[19] which were lower

than the melting temperature of bulk gold (1336 K).^[20] We observed that surface of gold nanoparticles melted first and consisted of disordered atoms while core remained ordered fcc structure (Figure 3D, 87 ps). During the neck formation, surface disordered atoms moved faster than ordered ones and touched each other (Figure 3D, 96 ps). Thus, necking region consisting of most disordered atoms (100 ps) was formed during merging. After merging, most of the disordered region changed to states of either stacking faults (red color) or original

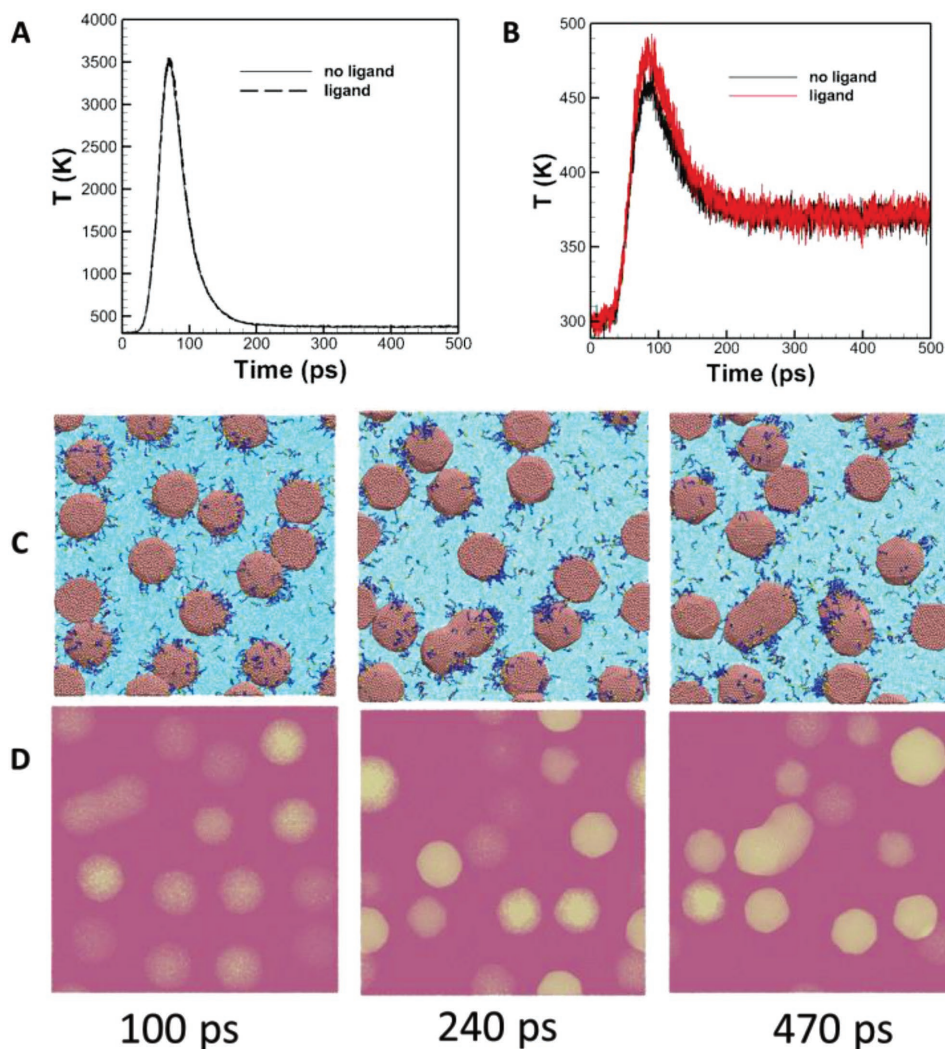


Figure 4. Nanocrystal transformation and merging in the presence of ligands on gold nanoparticle surface. A) Average gold nanoparticle temperature as a function of time at 120 mJ cm^{-2} for both ligand and without ligand cases. B) Average water temperature surrounding gold nanoparticles (within 0.5 nm distance to the surface of the gold nanoparticle) for both ligand and without ligand cases. C, D) Snapshot of gold nanoparticle merging at 3 nm interparticle distance with ligand and without ligand cases.

fcc orientation (green, 235 ps). Higher laser pulse fluence led to a thicker layer of disordered surface atoms and neck formation at earlier times (Figure S3, Supporting Information).

Next, we examined the effect of the surface ligand on the gold nanoparticle. Experimentally, the ligand–gold interface is the result of a reduction process by ascorbic acid. The ligand is physisorbed to the gold surface, as opposed to the chemisorbed case with a covalent bond. As a result, we used a model (see the Experimental Section for details) with a dissociation energy in the physisorbed regime ($1.38 \text{ kcal mol}^{-1}$). **Figure 4A** shows the average gold nanoparticle temperature history with laser fluence of 120 mJ cm^{-2} . The temperature profiles from both cases (with and without the ligands) are almost identical to each other. Further examination shows that the temperature of the water around gold nanoparticles are also similar (Figure 4B, averaged within 5 \AA to the gold surface). Thus, the presence of ligands produced negligible effect on the heat transfer at the gold/water interface. This is because during pulsed laser

heating, all the surface ligands were observed to quickly detach from the gold surface and move freely into the surrounding water layer. As a result, they did not bring a noticeable change in heat transfer. Subsequently, decoupled gold nanoparticles move in the ligand–water environment and merge. Snapshots of the merging of gold nanoparticles are shown in Figure 4C and are similar to the case without ligands (Figure 4D). Since the ligands have a negligible effect on the temperature history and completely detach from the gold nanoparticles, they are not considered in the following simulation studies.

To further investigate the mechanism of nanoparticle merging and transformation, we simulated a system of gold nanoparticles by removing water from the system. Surprisingly no merging of gold nanoparticles was observed (**Figure 5A**, at 30 mJ cm^{-2}). This indicates that water plays a critical role in merging the neighboring gold nanoparticles. To understand the role of water, we analyzed the motion of gold nanoparticles in the corresponding cases in the presence of water. Figure 5B

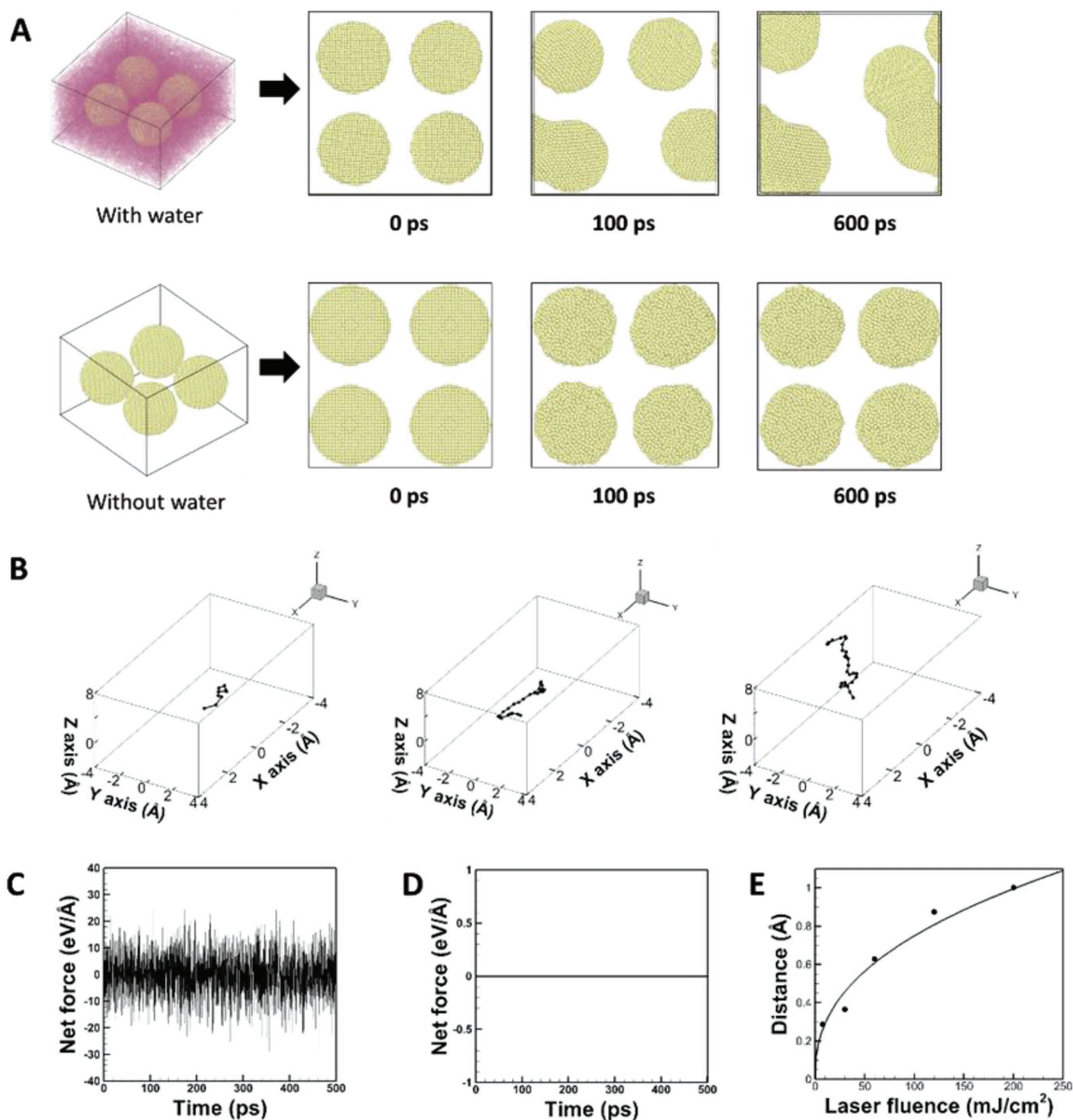


Figure 5. Nanocrystal transformation and merging are dependent on the presence of water and laser-induced nanoparticle motion. A) Snapshots of gold nanoparticles under laser pulse treatment with and without water at 30 mJ cm^{-2} and water molecules shown in semitransparent violet background. B) Trajectories of one representative gold nanoparticle for the first 300 ps when heated at different laser intensities (from left to right: no laser, 7.5 and 60 mJ cm^{-2}). C,D) Net force on gold nanoparticle with and without water at laser fluence of 30 mJ cm^{-2} . E) Nanoparticle traveling distance as a function of laser fluence for the first 24 ps. A correlation of $d \sim I_0^{0.41}$ best fits the data.

shows 3D trajectories of a single gold nanoparticle at 0 , 7.5 , and 60 mJ cm^{-2} . From the trajectories and comparison to the case without water, it is evident that gold nanoparticles were in Brownian motion due to the random forces exerted from the water molecules. This is further supported by the computed net force acting on a single nanoparticle for cases with water and

without water (Figure 5C,D). Net forces were close to zero in the absence of water, whereas a nonzero random net force triggered Brownian motion in the case with water.

Furthermore, the water-mediated Brownian motion is a function of laser fluence since the random forces depend on the kinetic temperature of the water molecules near the

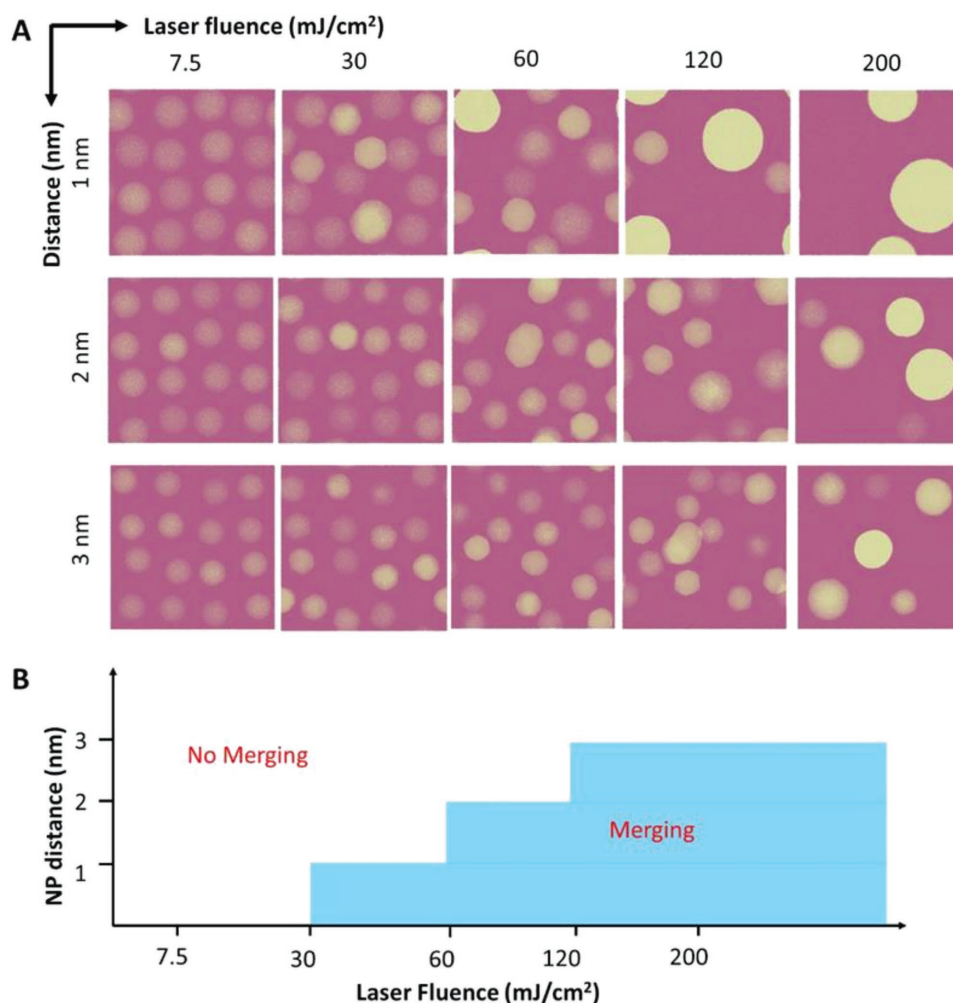


Figure 6. Combined effects of initial nanoparticle distance and laser fluence on the transformation and merging of gold nanoparticles. A) Snapshot and B) schematic diagram showing dependency of merging phenomena at 1, 2, and 3 nm initial distances and laser fluence values of 7.5, 30, 60, 120, and 200 mJ cm⁻². A top view is shown in (A) with water molecules shown in semitransparent background.

nanoparticle/water interfaces. To demonstrate this point, we provided a simple theoretical estimate on the distance (d) that the gold nanoparticle travels. This distance (d) is proportional to the magnitude of the net force f , which linearly scales with the kinetic velocity of the water molecule (v). Thus, d is related to the kinetic temperature of water (T) through $d \sim T^{1/2}$. If the initial temperature of the nanoparticles is 0 K, then T is linearly proportional to the laser fluence I_0 , from which we conclude that $d \sim I_0^{1/2}$. In the current application, the nanoparticles are suspended at room temperature with initial Brownian motion without laser pulse, leading to the conclusion that $d \sim I_0^n$ with $n < 0.5$. Figure 5E shows the nanoparticle distance as a function of the laser fluence and the simulation data yield the relation of $d \sim I_0^{0.41}$, which quantitatively describes the effects of the laser fluence and agrees with the theoretical estimate.

For the merging to take place, two gold nanoparticles under Brownian motion must come within a cutoff distance of 4.07 Å as defined by the interatomic potential. This means that equivalently a minimum distance of ≈ 6 Å must be travelled for merging with an initial inter-nanoparticle spacing of 10 Å,

which gives a net velocity of 20 m s⁻¹ assuming 30 ps duration. To verify the combined effects of the inter-nanoparticle distance and laser fluence, three inter-nanoparticle distances of 1, 2, and 3 nm were investigated along with laser fluences of 7.5, 30, 60, 120, and 200 mJ cm⁻². **Figure 6** shows that nanoparticle merging is strongly dependent on the inter-nanoparticle distance, and larger inter-nanoparticle distance requires higher laser fluence for the merging. Furthermore, careful examination of nanoparticle morphologies showed that merged nanoparticles were larger for smaller inter-nanoparticle distances. For instance, at 120 mJ cm⁻², merged nanoparticle with radius of 5.4 nm was observed at 1 nm inter-nanoparticle distance, while the radius is only ≈ 3.8 nm in the case of 3 nm inter-nanoparticle distance (Figure 6A). Figure 6B shows a schematic diagram that describes the combined effect of nanoparticle distance and laser fluence on the merging behavior.

The combined experimental and numerical investigation leads us to elucidate key factors that determine the nanocrystal transformation and nanoparticle merging. First, the nanoparticles have to be very close to each other for the merging to occur.

Previous studies have reported nanoparticle shape changes or fragmentation for nanoparticle dispersed in aqueous solutions,^[21] while nanoparticle merging or welding was only reported if the nanoparticles are chemically assembled into close proximity to each other.^[22] Our study further elucidates the effect of inter-nanoparticle distance, and reports that longer inter-nanoparticle distance requires higher laser fluence to merge the nanoparticles. Second, nanoparticle motion and the presence of water are critical for the nanoparticle merging and laser provides the driving force for enhanced Brownian motion. In the absence of water, no contact occurs while the nanoparticle is at a high temperature and no merging can take place. Finally, the effect of nanobubble nucleation and collapse on nanoparticle merging need further investigations. From our computational study, the nanoparticles merge within few hundred ps. On the other hand, the nanobubble nucleates on the order of nanoseconds and collapses after nucleation.^[11,23] The collapsing nanobubble creates nanojets^[24,25] and would not likely help nanoparticles to merge. Further work is required to investigate and clarify the effect of nanobubble collapse on the nanoparticle merging.

3. Conclusion

In summary, we have investigated the nanocrystal transformation in plasmonic vesicles under near-infrared laser pulse irradiation. This study identified key mechanisms in facilitating nanocrystal merging, including the nanocrystal melting and movement that lead to nanoparticle contact and subsequent merging. Major factors that control the nanocrystal merging include the laser fluence, the inter-nanoparticle distance, and the presence of water. This study shed light on important factors for plasmonic vesicle design and its successful biomedical applications that involve laser pulse irradiation. Furthermore, understandings derived from this study also address the feasibility of using laser pulses to weld different nanoparticles and thus provide new opportunities for the manufacturing of novel nanostructures that cannot be produced by wet chemical synthesis alone and made scalable.

4. Experimental and Computational Section

Plasmonic Vesicle Synthesis and Characterization: Liposomes were prepared from dipalmitoylphosphatidylcholine (DPPC) and cholesterol in a 4:1 molar ratio. Lipid powder was dispersed in chloroform (10×10^{-3} M lipid concentration) and dried by convection with N_2 , followed by overnight evaporation under vacuum. Dry lipid films were then dispersed in 10×10^{-3} M phosphate buffered saline (PBS) and subsequently extruded through 200 and 100 nm polycarbonate membranes for 21 passages. The reduction of gold onto the surface of liposomes was obtained by a previously reported method with minor revision as illustrated in Figure 1A.^[18] Briefly, gold chloride solution (10×10^{-3} M) was added into liposome suspension (1×10^{-3} M, lipid concentration) and gently mixed, followed by the addition of the ascorbic acid solution (40×10^{-3} M) and gentle mixing until color change was observed. Following reduction, each sample was dialyzed against PBS at 4 °C to remove unreacted materials. The size of uncoated liposomes and gold-coated liposomes was measured by dynamic light scattering. Uncoated and gold coated liposomes were photographed by transmission electron microscope (TEM, JEM-2100F, 200 keV) 24 h after fabrication at

1×10^{-3} M lipid concentration. Extinction spectra of uncoated liposomes and gold-coated liposomes were measured using a spectrophotometer. For laser treatment, gold-coated liposomes were flowed through a thin capillary and irradiated with a laser beam (750 nm wavelength, 28 ps pulse width, Altos Photonics). After laser irradiation, samples were collected for TEM imaging.

Computational Models for Gold Nanoparticles and Water: Figure 2 shows computational model setup of 16 gold nanoparticles surrounded by water. A small portion of the plasmonic vesicle for the simulation was selected. Each gold nanoparticle was 5 nm in diameter consisting of 3925 atoms. Surrounding water had 138 352 molecules. The simulation cell dimension was 24.8, 24.8, and 9.2 nm along the X, Y, and Z directions, respectively. The inter-nanoparticle distance was set at 1 nm initially and then changed to 2 and 3 nm in the parametric study. The dimension of the simulation cell was changed accordingly to accommodate the increased inter-nanoparticle distances. Periodic boundary condition was applied to all directions. Interactions among the gold atoms were described by embedded atom method (EAM) with parameters developed by Grochola et al.^[26] Water model used in this system was a three-site TIP3P.^[27] This model allows the water molecules to have bond stretching and angle bending. The bonded and nonbonded potentials used for water are described below

$$U_{\text{stretch}} = K_b (b - b_0)^2 \quad (1)$$

$$U_{\text{bend}} = K_\theta (\theta - \theta_0)^2 \quad (2)$$

$$U_{\text{Van der Waals}} = 4\epsilon \left[\left(\frac{\sigma}{r_{ij}} \right)^{12} - \left(\frac{\sigma}{r_{ij}} \right)^6 \right] \quad (3)$$

$$U_{\text{electrostatic}} = \frac{q_i q_j}{4\pi\epsilon_0 r_{ij}} \quad (4)$$

Here, U_{stretch} and U_{bend} are interatomic potential terms that correspond to bond stretching and angle bending, respectively. $U_{\text{Van der Waals}}$ describes the van der Waals interaction that is modeled by the Lennard-Jones (LJ) potential. $U_{\text{electrostatic}}$ accounts for the electrostatic interaction and is modeled with the Coulombic potential. The interaction between water and gold atoms was considered by prescribing a LJ 12-6 interaction between oxygen and gold atoms.^[28] A cutoff radius of 10 Å was considered in the LJ potential to reduce the computational cost. Table S1 (Supporting Information) provides the parameter list used in TIP3P with a long-range Coulombic solver.^[29]

To investigate the possible role of molecular ligands on the gold nanoparticle surface toward heat transfer and gold nanoparticle merging, a hydroxyl-terminated alkanethiol ligand (Figure S4, Supporting Information, $\text{SH}-(\text{CH}_2)_{10}-\text{OH}$) was modeled by adjusting the dissociation energy to match physisorbed ligands. One advantage to model this ligand is because the modeling of alkanethiol ligands is a well-understood topic with straightforward protocols.^[30,31] The protocol of Ghorai and Glotzer,^[30] including the use of an Au-S Morse potential to attach ligands to the gold nanoparticle, was followed. Three modifications were made: (1) we used the CHARMM General Force Field (CGenFF) for the ligand parameters, (2) we prepared gold nanoparticles with several different ligand surface densities, and (3) we adjusted the Morse potential dissociation energy to be in the physisorbed energy regime (since the citrate ligands used experimentally are physisorbed to the gold surface). For each ligand surface density, we placed the ligands uniformly around the gold nanoparticles. The interaction between gold and sulfur atoms in the ligand molecules is described by a Morse potential

$$E = D_0 \left[e^{-2\alpha(r-r_0)} - 2e^{-\alpha(r-r_0)} \right] \quad (5)$$

where D_0 is the well depth, α controls the width of the potential, r is the distance between two atoms, and r_0 is the equilibrium bond distance.

Coupled Electromagnetic/Molecular Dynamics Simulation Setup: All the molecular dynamics simulations were performed using LAMMPS package.^[32] At first, potential energy of the gold–water system was minimized using conjugate gradient algorithm. After that, the system was thermodynamically equilibrated at 300 K and 1 atm pressure for 250 ps using isothermal–isobaric (*NPT*) ensemble to maintain overall temperature of 300 K, which means that the gold–water system is under atmospheric conditions. To simulate the heating of nanoparticle by the laser pulse, an absorbed power density was applied at each atom site based on the electromagnetic field calculated from DDA. This absorbed power density, $q_j(t)$, can be expressed as^[33]

$$q_j(t) = \frac{2\pi\epsilon_2 \epsilon_{2j,\lambda}}{n_s \lambda_0} R_{j,\lambda} I(t) \quad (6)$$

where n_s is the refractive index of medium surrounding the nanoparticle ($=1.33$ for water), λ_0 is the vacuum wavelength of incident light, $\epsilon_{2j,\lambda}$ is the imaginary part of the dielectric function at the wavelength λ , $R_{j,\lambda}$ is the square electric field ratio at the grid point j computed from DDA method, and $I(t)$ is the instantaneous incident laser intensity onto the nanoparticle. Gaussian profile is assumed for the prescribed laser intensity $I(t)$ and expressed as

$$I(t) = \frac{I_0}{\tau} \exp\left[-2.77\left(\frac{t-2\tau}{\tau}\right)^2\right] \quad (7)$$

Here, I_0 is the laser fluence in mJ cm^{-2} , τ is the pulse duration ($=28$ ps), and t is the time. Temperature of the system is calculated by the following equation

$$KE = \frac{\text{dim}}{2} nKT \quad (8)$$

where KE is the kinetic energy of the group of atoms, dim is the dimensionality of the simulation, n is the number of group of atoms, K is the Boltzmann constant, and T is the temperature.

Dielectric Functions of Gold Nanoparticles: Dielectric functions are required in the electromagnetic field calculation. Dielectric function of nanostructures $\epsilon(a,\omega)$ is given based on the Drude permittivity model^[34,35]

$$\epsilon(a,\omega) = \epsilon_{\text{bulk}}(\omega) + \frac{\omega_p^2}{\omega^2 + i\omega\gamma_{\text{bulk}}} - \frac{\omega_p^2}{\omega^2 + i\omega\gamma(L_{\text{eff}})} \quad (9)$$

where $\epsilon_{\text{bulk}}(\omega)$ is the bulk dielectric function of gold measured from experiment,^[36] γ_{bulk} is the electron collision frequency, and ω_p ($=1.3 \times 10^{15}$ Hz) is the plasmon frequency of gold.^[37] $\gamma(L_{\text{eff}})$ is the size-dependent damping constant of electrons^[34]

$$\gamma(L_{\text{eff}}) = \gamma_{\text{bulk}} + A \frac{v_F}{L_{\text{eff}}} \quad (10)$$

where v_F is the Fermi velocity, A is a scattering parameter (≈ 0.8 for very small gold nanoparticles in the range 2–3 nm^[37]), and L_{eff} ($=1.33a$ for spherical nanoparticle of radius a) is effective length of electron-boundary scattering.^[34,35] The temperature may affect the dielectric function of gold as pointed out by Chen et al.^[38] According to the Drude model, it has been shown that the most temperature-dependent parameters are the plasmon frequency (about 13.8×10^{15} rad s^{-1} at 300 K but decreasing to 10.5×10^{15} rad s^{-1} at 800 K) and the electron damping constant (about 0.17×10^{15} s^{-1} at 300 K and increasing to 0.66×10^{15} s^{-1} at 800 K). The effect of the temperature on the optical properties of 5 nm gold nanoparticle was studied by comparing computed absorption efficiency factor at the plasmon peak wavelength at room temperature and at 800 K. It was found that the absorption efficiency at 300 K is about 0.498 while it increases slightly to 0.518 at 800 K, or 4% change. It is expected that higher temperature will lead to slightly higher absorbed power density but given the small effect of temperature on absorption characteristics of 5 nm gold nanoparticles, the temperature dependence of the dielectric function is neglected.

It is important to note that there are differences in the dipole and atom arrangements (cubic vs face centered cubic) and the sizes of dipole and gold lattice parameters (dipole size is 0.1 nm while the gold lattice parameter is 0.47 nm). Thus, the electric field data from DDA simulation are mapped to the sites of gold atoms in MD simulation using hexahedral interpolation scheme, developed in finite element method.^[39]

DDA to Calculate Electromagnetic Field Distribution: DDA is a discrete solution method of the integral form of Maxwell's equations and allows the prediction of nanostructure optical properties with complex geometries.^[40] The DDA method was described in detail elsewhere.^[41,42] Briefly, the structure (gold nanoparticle surrounded by water here) is discretized into a finite array of dipoles (N) with each dipole located at position vector \vec{r}_j ($j = 1, N$). Figure S5 (Supporting Information) reports the model system used in the DDA calculation. It is worth noting that nanoparticle distance may affect collective optical properties of plasmonic vesicle and in turn affects the photothermal effect.^[43] It was observed that when gold nanoparticles are sufficiently close or to overlap, the nanoparticle plasmon wave coupling becomes effective. Specifically, for the case of nanoparticle gap of 1 nm, a weak interaction of nanoparticle plasmons takes place via Coulomb interaction of opposite charges. Therefore, the power density was computed considering a cluster of uniformly distributed nanoparticles configured as shown in Figure S5A (Supporting Information). For the cases of large nanoparticle gaps (i.e., gaps of 2 and 3 nm), plasmonic coupling is not effective. Therefore, the absorbed power density was computed from a single nanoparticle configuration as shown in Figure S5B (Supporting Information). With the DDA method, the solution to the electromagnetic wave problem is reduced to solving a system of $3N$ complex linear equations with $3N$ unknowns that are the dipole moment vectors \vec{P}_j ($j = 1, N$)^[41]

$$\sum_{i=1}^N \mathbf{A}_{ji} \vec{P}_i = \vec{E}_{\text{inc},j} \quad (11)$$

where \vec{P}_i is the dipole moment vector, and \mathbf{A}_{ji} is a 3×3 complex symmetric matrix, with its elements depending on the wavelength λ and the vector distance between dipoles j and i , $\vec{r}_i - \vec{r}_j$. $\vec{E}_{\text{inc},j}$ is the incident field vector at dipole j . Once the system of Equation (11) is solved, the far-field (absorption, extinction, scattering, Muller matrix elements, etc.) and near-field properties can be computed. For instance, the absorption cross section is obtained from^[41]

$$C_{\text{abs}} = \frac{8\pi^2}{E_{\text{inc}}^2 \lambda} \sum_{j=1}^N \left\{ \text{Im} \left[\vec{P}_j^* \cdot (\alpha_j^{-1})^* \cdot \vec{P}_j \right] - \frac{2}{3} \eta^3 |\vec{P}_j|^2 \right\} \quad (12)$$

where E_{inc} is the amplitude of the incident electric field. α_j is the polarizability of the dipole j . The electromagnetic field at any dipole site j is computed by

$$\vec{E}_j = \vec{E}_{\text{inc},j} - \sum_{i=1}^N \mathbf{A}_{ji} \vec{P}_i \quad (13)$$

Square electric field ratio at j grid point is denoted by $R_j = |\vec{E}_j|^2 / |\vec{E}_{\text{inc},j}|^2$. These data are interpolated using eight-node hexahedral isoparametric element^[39] as an input for Equation (6) in the atomistic simulations by the following equation

$$R_{j,\lambda} = \sum_{j=1}^n \bar{N}_j R_j \quad (14)$$

where \bar{N}_j is the shape function of the eight-node hexahedral element.^[39]

In this study, the DDA package DDSCAT 7.3.1 developed by Draine and Flatau^[41,44] was implemented. Gold nanoparticles were discretized in regular arrays of N dipoles of spacing d , while the water was taken into account implicitly as a surrounding medium. The dipoles are characterized by the frequency-dependent dielectric function $\epsilon(a,\omega)$.

The dipole spacing should be small as compared to any structural length in the target geometry, and the wavelength of the electromagnetic wavelength, λ . A convenient “rule of thumb” developed to satisfy these criteria is^[41,42]

$$|m| \frac{2\pi d}{\lambda} < 0.5 \quad (15)$$

Here, m is the ratio of complex refractive index of the gold spheres ($n_{\text{NP}} = \sqrt{\epsilon(\mathbf{a}, \omega)}$) to that of the surrounding water $n_{\text{water}} = 1.33$. In practice, even if Equation (15) is satisfied, the dipole size d is further refined so that the computational results converge over the spectral range of interest. Analysis of the dipole size effect on extinction efficiency factor over the visible and near-infrared spectrum was performed by comparing the DDA results with available experimental data for 3.2 nm nanoparticle size (Figure S6, Supporting Information). Based on this analysis, a dipole size of 0.1 nm was used in the DDA simulation of 5 nm nanoparticle. Additionally, the model does not take into account nonlocal effect since continuum dielectric function is used.^[43] The hypothesis is validated by successful comparison between experimental data of optical properties of very small nanoparticles (3.2 nm) and calculation using continuum dielectric function (Figure S6, Supporting Information).

Supporting Information

Supporting Information is available from the Wiley Online Library or from the author.

Acknowledgements

This study was partially supported by a Cancer Prevention and Research Institute of Texas grant to Z.Q. (CPRIT, RP160770), National Science Foundation grants to Z.Q. (1631910) and to D.Q. (1727960), a postdoc research grant from the Phospholipid Research Center (Heidelberg, Germany) to X.L. (1603574), and startup fund from The University of Texas at Dallas to Z.Q. J.R. acknowledges UT Dallas for hosting his visit at Z.Q. Lab. The authors gratefully acknowledge the High-performance Computing (HPC) resources that were employed for this research and made available through the Texas Advanced Computing Center (TACC) at The University of Texas at Austin, ROMEO Computing Center hosted by the University of Reims Champagne-Ardenne, and the Extreme Science and Engineering Discovery Environment (XSEDE) which was supported by National Science Foundation (Grant No. ACI-1053575).

Conflict of Interest

The authors declare no conflict of interest.

Keywords

atomistic simulation, discrete dipole approximation, gold nanoparticles, ligands

Received: June 4, 2018
Revised: August 3, 2018
Published online:

- [1] A. Albanese, P. S. Tang, W. C. W. Chan, *Annu. Rev. Biomed. Eng.* **2012**, *14*, 1.
[2] L. Y. T. Chou, K. Zagorovsky, W. C. W. Chan, *Nat. Nanotechnol.* **2014**, *9*, 148.
[3] T. S. Troutman, S. J. Leung, M. Romanowski, *Adv. Mater.* **2009**, *21*, 2334.
[4] P. Huang, J. Lin, W. Li, P. Rong, Z. Wang, S. Wang, X. Wang, X. Sun, M. Aronova, G. Niu, R. D. Leapman, Z. Nie, X. Chen, *Angew. Chem., Int. Ed.* **2013**, *52*, 13958.

- [5] Y. Liu, J. He, K. Yang, C. Yi, Y. Liu, L. Nie, N. M. Khashab, X. Chen, Z. Nie, *Angew. Chem., Int. Ed.* **2015**, *54*, 15809.
[6] A. K. Rengan, M. Jagtap, A. De, R. Banerjee, R. Srivastava, *Nanoscale* **2014**, *6*, 916.
[7] S. J. Leung, M. Romanowski, *Theranostics* **2012**, *2*, 1020.
[8] R. Qian, Y. Cao, Y.-T. Long, *Angew. Chem., Int. Ed.* **2016**, *55*, 719.
[9] A. K. Rengan, A. B. Bukhari, A. Pradhan, R. Malhotra, R. Banerjee, R. Srivastava, A. De, *Nano Lett.* **2015**, *15*, 842.
[10] J. Liu, M. Yu, C. Zhou, J. Zheng, *Mater. Today* **2013**, *16*, 477.
[11] X. Li, Z. Che, K. Mazhar, T. J. Price, Z. Qin, *Adv. Funct. Mater.* **2017**, *27*, 1605778.
[12] G. González-Rubio, A. Guerrero-Martínez, L. M. Liz-Marzán, *Acc. Chem. Res.* **2016**, *49*, 678.
[13] S. K.-M. Lai, H.-W. Tang, K.-C. Lau, K.-M. Ng, *J. Phys. Chem. C* **2016**, *120*, 20368.
[14] Y. Li, Z. Jiang, X.-M. Lin, H. Wen, D. A. Walko, S. A. Deshmukh, R. Subbaraman, S. K. R. S. Sankaranarayanan, S. K. Gray, P. Ho, *Sci. Rep.* **2015**, *5*, 8146.
[15] J. Fontana, N. Charipar, S. R. Flom, J. Naciri, A. Piqué, B. R. Ratna, *ACS Photonics* **2016**, *3*, 904.
[16] G. González-Rubio, P. Díaz-Núñez, A. Rivera, A. Prada, G. Tardajos, J. González-Izquierdo, L. Bañares, P. Llombart, L. G. Macdowell, M. A. Palafox, L. M. Liz-Marzán, O. Peña-Rodríguez, A. Guerrero-Martínez, *Science* **2017**, *358*, 640.
[17] T. Tsuji, T. Yahata, M. Yasutomo, K. Igawa, M. Tsuji, Y. Ishikawa, N. Koshizaki, *Phys. Chem. Chem. Phys.* **2013**, *15*, 3099.
[18] B. Dragnea, C. Chen, E.-S. Kwak, B. Stein, C. C. Kao, *J. Am. Chem. Soc.* **2003**, *125*, 6374.
[19] J.-H. Shim, B.-J. Lee, Y. W. Cho, *Surf. Sci.* **2002**, *512*, 262.
[20] Z. Qiao, H. Feng, J. Zhou, *Phase Transitions* **2014**, *87*, 59.
[21] D. Zhang, B. Gökce, S. Barcikowski, *Chem. Rev.* **2017**, *117*, 3990.
[22] A. Babynina, M. Fedoruk, P. Kühler, A. Meledin, M. Döblinger, T. Lohmüller, *Nano Lett.* **2016**, *16*, 6485.
[23] A. Siems, S. Weber, J. Boneberg, A. Plech, *New J. Phys.* **2011**, *13*, 043018.
[24] D. Sun, X. Lin, Z. Zhang, N. Gu, *J. Phys. Chem. C* **2016**, *120*, 18803.
[25] M. Vedadi, A. Choubey, K.-I. Nomura, R. Kalia, A. Nakano, P. Vashishta, A. van Duin, *Phys. Rev. Lett.* **2010**, *105*, 014503.
[26] G. Grochola, S. P. Russo, I. K. Snook, *J. Chem. Phys.* **2005**, *123*, 204719.
[27] W. L. Jorgensen, J. Chandrasekhar, J. D. Madura, R. W. Impey, M. L. Klein, *J. Chem. Phys.* **1983**, *79*, 926.
[28] S. Merabia, S. Shenogin, L. Joly, P. Keblinski, J.-L. Barrat, *Proc. Natl. Acad. Sci. USA* **2009**, *106*, 15113.
[29] D. J. Price, C. L. Brooks III, *J. Chem. Phys.* **2004**, *121*, 10096.
[30] P. K. Ghorai, S. C. Glotzer, *J. Phys. Chem. C* **2007**, *111*, 15857.
[31] S. Monti, G. Barcaro, L. Sementa, V. Carravetta, H. Agren, *RSC Adv.* **2017**, *7*, 49655.
[32] S. Plimpton, *J. Comput. Phys.* **1995**, *117*, 1.
[33] G. Baffou, R. Quidant, *Laser Photonics Rev.* **2013**, *7*, 171.
[34] Z. Qin, Y. Wang, J. Randrianalisoa, V. Raeesi, W. C. W. Chan, W. Lipiński, J. C. Bischof, *Sci. Rep.* **2016**, *6*, 29836.
[35] E. A. Coronado, G. C. Schatz, *J. Chem. Phys.* **2003**, *119*, 3926.
[36] P. B. Johnson, R. W. Christy, *Phys. Rev. B* **1972**, *6*, 4370.
[37] B. S. Lucía, O. T. Jorge, *Nanotechnology* **2006**, *17*, 1309.
[38] Y.-J. Chen, M.-C. Lee, C.-M. Wang, *Jpn. J. Appl. Phys.* **2014**, *53*, 08MG02.
[39] R. D. Cook, D. S. Malkus, M. E. Plesha, R. J. Witt, *Concepts and Applications of Finite Element Analysis*, Wiley, New York **1974**.
[40] J. Randrianalisoa, W. Lipiński, *Appl. Opt.* **2014**, *53*, 1290.
[41] B. T. Draine, P. J. Flatau, *J. Opt. Soc. Am. A* **1994**, *11*, 1491.
[42] M. A. Yurkin, A. G. Hoekstra, *J. Quant. Spectrosc. Radiat. Transfer* **2007**, *106*, 558.
[43] J. Randrianalisoa, X. Li, M. Serre, Z. Qin, *Adv. Opt. Mater.* **2017**, *5*, 1700089.
[44] P. J. Flatau, B. T. Draine, *Opt. Express* **2012**, *20*, 1247.